

1 **Structural and biochemical characterization of endoribonuclease Nsp15**
2 **encoded by Middle East respiratory syndrome coronavirus**

3

4 **Running title: Crystal structure of MERS-CoV Nsp15**

5

6 **Lianqi Zhang^{1‡}, Lei Li^{2‡}, Liming Yan¹, Zhenhua Ming³, Zhihui Jia¹, Zhiyong Lou¹**
7 **and Zihe Rao^{1,4,5*}**

8

9 ¹Laboratory of Structural Biology, School of Medicine, Tsinghua University, Beijing
10 100084, China.

11 ²State Key Laboratory of Biotherapy/Collaborative Innovation Center for Biotherapy,
12 West China Hospital, Sichuan University, Chengdu, Sichuan, China

13 ³State Key Laboratory of Conservation and Utilization of Subtropical Agro-Bioresources,
14 College of Life Science and Technology, Guangxi University, Nanning, China

15 ⁴National Laboratory of Macromolecules, Institute of Biophysics, Chinese Academy of
16 Science, Beijing 100101, China

17 ⁵College of Life Sciences, Nankai University, Tianjin 300071, China

18

19 ***Corresponding author:** Zihe Rao, raozh@mail.tsinghua.edu.cn

20 [‡] Lianqi Zhang and Lei Li contributed equally to this work.

21

22 **Key words:** MERS-CoV, endoribonuclease, crystal structure, oligomerization

23

24 **Word counts:** Abstract: 233; Importance: 102; Main text: 5596 (excluding references
25 and legends)

26

27

28 **ABSTRACT**

29 Non-structural protein 15 (Nsp15) encoded by coronavirus (CoV) is a uridylyate specific
30 endoribonuclease (NendoU) that plays an essential role in the life cycle of the virus.

31 Structural information of this crucial protein from the Middle East respiratory syndrome
32 (MERS) CoV, which is lethally pathogenic and has caused severe respiratory diseases
33 worldwide, is lacking. Here, we report the crystal structure of MERS-CoV Nsp15 at a 2.7

34 Å resolution and perform the relevant biochemical assays to study how NendoU activity
35 is regulated. Although the overall structure is conserved, MERS-CoV Nsp15 shows
36 unique and novel features compared to its homologs. Serine substitution of residue F285,

37 which harbors an aromatic side chain that disturbs RNA binding compared with other
38 homologs, increases catalytic activity. Mutations of residues residing on the
39 oligomerization interfaces that distort hexamerization, namely, N38A, Y58A and N157A,

40 decrease thermostability, decrease binding affinity with RNA and reduce the NendoU
41 activity of Nsp15. In contrast, mutant D39A exhibits increased activity and a higher
42 substrate binding capacity. Importantly, Nsp8 is found to interact with both monomeric

43 and hexameric Nsp15. The Nsp7/Nsp8 complex displays a higher binding affinity for

44 Nsp15. Furthermore, Nsp8 and the Nsp7/Nsp8 complex also enhance the NendoU
45 activity of hexameric Nsp15 *in vitro*. Taken together, this work first provides evidence on
46 how the activity of Nsp15 may be functionally mediated by catalytic residues, oligomeric
47 assembly, RNA binding efficiency or the possible association with other non-structural
48 proteins.

49

50 **IMPORTANCE**

51 The lethally pathogenic Middle East respiratory syndrome coronavirus (MERS-CoV) and
52 the severe acute respiratory syndrome coronavirus (SARS-CoV) pose serious threats to
53 humans. Endoribonuclease Nsp15 encoded by coronavirus plays an important role in
54 viral infection and pathogenesis. This study determines the structure of MERS-CoV
55 Nsp15 and demonstrates how the catalytic activity of this protein is potentially mediated,
56 thereby providing structural and functional evidence for developing antiviral drugs. We
57 also hypothesize that the primase-like protein Nsp8 and Nsp7/Nsp8 complex may interact
58 with Nsp15 and affect enzymatic activity. This contributes to the understanding of the
59 association of Nsp15 with the viral replication and transcription machinery.

60

61

62

63

64

65 **INTRODUCTION**

66 A decade after the severe acute respiratory syndrome coronavirus (SARS-CoV) epidemic,
67 a zoonotic coronavirus called the Middle East respiratory syndrome coronavirus
68 (MERS-CoV) circulated throughout the human population (1, 2). The lack of
69 CoV-specific anti-viral drugs or an effective vaccine has severely hampered efforts to
70 combat the spread of this virus. It is therefore important to study the life cycle of the virus
71 and the role viral proteins play in its propagation so that they can be targeted for the
72 development of anti-viral therapeutics.

73 CoVs are enveloped, single-stranded positive RNA viruses (3). The genomes of CoVs are
74 the largest among RNA viruses and range between 26 and 32 kb (4). Almost two-thirds of
75 the genome encompasses two large open reading frames (ORFs), ORF 1a and ORF 1b,
76 which encode 16 non-structural proteins (Nsps) that play essential roles in coronavirus
77 RNA replication and transcription. A unique feature shared by all CoVs is that the
78 ribosome undergoes a -1 frameshift following the translation of Nsp10. This results in the
79 production of a large polypeptide, 1ab, that is then proteolytically processed to produce
80 the 16 viral Nsps (5, 6). In addition to these Nsps, several structural and accessory
81 proteins are synthesized from ORFs located at the 3' end of the viral genome. These
82 ORFs are transcribed into a nested set of subgenomic RNAs that are ultimately translated
83 into structural proteins (7, 8).

84 Non-structural protein 15 (Nsp15) is a nidoviral uridylyate specific endoribonuclease
85 (NendoU) (9). It was reported to preferentially cleave 3' of uridylyates over cytidylates
86 and generate a 2',3'-cyclic phosphate and 5'-OH ends (10). The activities of SARS-CoV
87 Nsp15 and mouse hepatitis virus (MHV) Nsp15 were reported to be significantly
88 stimulated by Mn^{2+} (11-12). Previous studies have demonstrated that the recombinant

89 SARS-CoV Nsp15 and MHV Nsp15 both existed in a monomer-trimer-hexamer
90 equilibrium in solution, with the hexamer possessing endoribonuclease activity (10,
91 12-14). Crystal structures of Nsp15 from SARS-CoV and MHV reveal that
92 hexamerization of the protein lends structural support to maintain integrity of the active
93 site. Two loops in the catalytic domain (residues 234-249 and 276-295 in SARS-CoV
94 Nsp15) are packed against each other and are stabilized by intimate inter-monomer
95 interactions (12-14). N-terminal truncation of SARS-CoV Nsp15 resulted in an inactive
96 monomeric state, with the catalytic loop containing two catalytic residues, H234 and
97 H249, falling into the active site cleft (15), which provides structural evidence to support
98 that the hexamer is the active form.

99 Several *in vivo* studies have also been conducted to evaluate the function of Nsp15.
100 Loss-of-function mutations in the catalytic sites of MHV Nsp15 reduced subgenomic
101 RNA accumulation and profoundly attenuated virus infection, and similar results were
102 also observed with SARS-CoV and Arterivirus (16, 19, 21). More recently, Nsp15 from
103 SARS-CoV was found to be an inhibitor of mitochondrial antiviral signaling adaptor
104 (MAVS) inducing apoptosis (17). In addition, Nsp15 from both MHV and SARS-CoV
105 can interact with retinoblastoma tumor suppressor protein (pRb), thus affecting cell
106 cycle-associated gene expressions (18). It is therefore likely that Nsp15 impacts not only
107 the viral life cycle but also the metabolic status and immune response of the host cells.
108 Moreover, MHV Nsp15 has been demonstrated to colocalize and interact with the viral
109 primase Nsp8 and polymerase Nsp12 *in vivo* (20), suggesting its possible involvement in
110 RNA replication and transcription.

111 Here, we first describe the crystal structure of Nsp15 from MERS-CoV refined to a 2.7 Å
112 resolution. Crucial residues within the active site pocket and interprotomer interaction

113 surfaces played essential roles in the enzymatic function of the protein by directly
114 regulating catalysis or imparting oligomeric arrangement and stability, thus modulating
115 the substrate-RNA binding process. Furthermore, we demonstrated that primase-like
116 Nsp8 and the Nsp7/Nsp8 complex could interact with MERS-Nsp15 and affect NendoU
117 activity, indicating a possible association of Nsp15 with other important non-structural
118 proteins that are involved in RNA replication and transcription.

119

120

121 **RESULTS**

122 **Overall structure of MERS-CoV Nsp15**

123 The recombinant full-length MERS-CoV Nsp15 was expressed, purified to homogeneity,
124 crystallized in the *H3* space group and diffracted to a 2.7 Å resolution. The final
125 coordinates consist of protein residues 1-341 with good crystallographic quality (Table
126 1). For simplicity, MERS-Nsp15 and SARS-Nsp15 are used to represent MERS-CoV
127 Nsp15 and SARS-CoV Nsp15, respectively, in this paper.

128 The overall structure of MERS-Nsp15 consists of three distinct domains (Fig. 1A) and
129 shares homology with the reported SARS-Nsp15 and MHV Nsp15 (12-14). Residues 1 to
130 60 are folded into a small N-terminal domain, in which three anti-parallel β -strands
131 (β 1- β 3) are observed forming a curved β -sheet with two short α -helices (α 1, α 2) right
132 beneath it. The N-terminal domain is followed by a middle domain that contains a central
133 β -sheet (β 4, β 7, β 8, β 11) flanked by two small α -helices (α 3, α 4) on either side. Two
134 short β -strands (β 9- β 10) arranged in a β -hairpin are located at the interface of the central
135 domain and the C-terminal domain. Residues I190 to R341 within the C-terminal domain
136 pack into two β -sheets consisting of β -strands β 13- β 15 and β -strands β 16- β 18, which

137 constitute the catalytic site cleft located at one side of the C-terminal domain. A group of
138 five small α -helices ($\alpha 5$ - $\alpha 9$) packed at the other side of the domain face the concave
139 surface of the β -sheets.

140 Crystal packing of MERS-Nsp15 is suggestive of a hexamer model. A dimer of trimers
141 that constitutes a hexameric architecture with the crystallographic three-fold axis passing
142 through the center of the hexameric assembly (Fig. 1B-C). The N-terminal domains of
143 the protomers within the two trimers pack back-to-back into a hexamer, placing the
144 C-terminal domains that harbour the active site at the apexes of the cloverleaf-like
145 symmetry (Fig. 1C). Within the trimer assembly, the N-terminal domain of one protomer
146 packs with a cleft between the central domain and the C-terminal domain of an adjacent
147 protomer (Fig. 1C).

148 The structure of Nsp15 is conserved, with the root mean square deviations (r.m.s.d.) of
149 $C\alpha$ atoms at 1.23 Å and 1.17 Å between monomeric MERS-Nsp15 and SARS-Nsp15 as
150 well as MHV Nsp15. The r.m.s.d. for comparison of the trimeric MERS-Nsp15 with
151 SARS-Nsp15 and MHV Nsp15 is 2.49 Å and 3.02 Å, respectively (Fig. 2A). Three
152 domains within the monomer are also conserved, with r.m.s.d. of $C\alpha$ atoms of aligned
153 residues ranging from 0.71-1.25 Å (Fig. 2B). Additionally, many of the conserved
154 residues that may contribute to the function of the protein (key residues that make up the
155 catalytic site within the C-terminal domain and polar residues forming hydrogen bond
156 networks) may be essential for protein function (Fig. 3).

157

158 **Key residues within the catalytic site**

159 To better uncover the structural information within the catalytic site, the structures of
160 MERS-Nsp15 and SARS-Nsp15 were superimposed (Fig. 4A). Three highly conserved

161 residues clustering in a positively charged groove are known to drive NendoU-mediated
162 catalysis: the two catalytic histidines, H231 and H246, are located on a long, convoluted
163 loop wedged between two adjacent β -sheets, and the third catalytic residue, K286, resides
164 on strand- β 15. The spatial arrangements reveal that residues S290 and Y339 in
165 MERS-Nsp15 correspond to residues S293 and Y342 in SARS-Nsp15, which are
166 postulated to interact with substrate and confer uridylate specificity (14), suggesting that
167 there is conserved recognition for uridylate. However, not all residues within the active
168 site are conserved among coronaviruses. Several notable differences include the
169 phenylalanine (F285) in MERS-Nsp15 that is located on strand- β 15 within one of the 2
170 β -sheets at one end of the catalytic site. The aromatic side chain of F285 protrudes
171 outward at a roughly perpendicular angle to the β -strand plane, compared to the
172 corresponding serine (S288) in SARS-Nsp15. A threonine (T241), which is spatially
173 located next to F285 and H246, occupies the position of Q244 in SARS-Nsp15, whereas
174 an isoleucine is located in the corresponding position in MHV-Nsp15 (Fig. 3, Fig. 4A). In
175 addition, an arginine (R341) in MERS-Nsp15 replaces a lysine (K344) in SARS-Nsp15
176 (Fig. 3). Thus, residues that are not conserved revealed unique features in MERS-Nsp15.

177

178 **Functional characterization of MERS-Nsp15 and its active site mutants**

179 To explore the functional importance of residues within the catalytic site, the residues
180 listed in Fig. 4A were substituted by alanine. Gel filtration revealed that all mutants
181 shared similar elution profiles to that of the wild-type Nsp15. The elution profiles
182 exhibited a dominant peak corresponding to a hexamer (data not shown). To further
183 investigate the thermostability of these mutants, we conducted differential scanning
184 fluorimetry (DSF) assay, which has been used to assess interactions among protein

185 subunits (22). The denaturation profile of wild-type Nsp15 and its mutants in Fig. 4A
186 revealed that they all exhibited a major transition at the melting temperature (T_m) of 46
187 °C, which is suggestive of a native fold (Fig. 4C). Taken together, the mutation of key
188 residues in the active site had no effect on the oligomeric assembly and stability of
189 MERS-Nsp15.

190 We subsequently investigated the NendoU activity of these active-site mutants using
191 fluorescent resonance energy transfer (FRET) assays, in which a substrate containing a
192 nucleotide rU was used. Alanine substitution of the three highly conserved residues
193 (H231, H246 and K286), as well as the residues located in the immediate surrounding
194 regions (Y339, T241 and R341), decreased ribonuclease activity to background level
195 (Fig. 4D-E). Notably, when T241 was substituted with the corresponding residue
196 glutamine in SARS-Nsp15, T241Q exhibited wild-type activity. Mutating R341 to lysine,
197 the corresponding residue in SARS-Nsp15, decreased NendoU activity to approximately
198 50 % of wild-type protein activity (Fig. 4E). Interestingly, the catalytic rate of Nsp15
199 slightly increased to $1.34 \pm 0.06 \text{ nM s}^{-1}$ when F285 was substituted by alanine, which is
200 found in the equivalent position in EAV (equine arteritis virus) (Fig. 4). We also replaced
201 F285 with a serine, a residue that is present in all other coronaviruses at this position.
202 Serine substitution resulted in an increase in catalytic activity to $1.63 \pm 0.07 \text{ nM s}^{-1}$ (Fig.
203 4E). Moreover, alanine substitution of S290, for which the corresponding residue was
204 postulated to confer uridylate specificity, abolished the activity to 67 % of the wild-type
205 Nsp15 activity (Fig. 4D).

206 How does the disruption of active-site residues affect NendoU activity? We next used
207 fluorescence polarization (FP) assay to assess the RNA binding ability of these mutants.

208 Three different RNAs (R1-R3) are designed to identify the one that binds the strongest to
209 Nsp15: R1 contains 20 rU; R2 is derived from the conserved transcriptional regulatory
210 sequence (TRS) of the viral genome; and R3 is a double-stranded RNA annealed by R2
211 and its complementary strand. Among the three oligomers, Nsp15 exhibited the highest
212 binding affinity to RNA R1 (Fig. 4B). RNA R1 also had the highest inhibitory effect on
213 NendoU activity in the FRET-based assays, suggesting that it possesses the strongest
214 binding ability, and was thus used in all FP assays to assess the RNA-Nsp15 interactions
215 in this paper (Fig. 4B). Mutants K286A, H246A, H231A, Y339A, T241A and R341A,
216 which exhibited no activity, were all able to bind RNA, indicating that their decreased
217 activity was not caused by substrate binding, but possibly by the directly catalytic
218 function of these residues (Table 2). Of note, the F285A and F285S mutants exhibited
219 stronger binding compared to the wild-type protein, which may explain why the NendoU
220 activity of these two mutants increased (Fig. 4E, Table 2). Consistently, mutant S290A,
221 which exhibited partly diminished activity, conferred a moderate decrease in RNA
222 binding ability. In conclusion, these observations corroborated that mutation of critical
223 residues within the active site, through either directly disrupting catalysis or impacting
224 RNA binding affinity, may influence NendoU activity.

225

226 **Oligomeric assembly affects RNA binding and NendoU activity**

227 To gain insight into the correlation between NendoU activity and the distinct oligomeric
228 forms, we examined the interprotomer surfaces and disrupted several key residues that
229 contribute to the hydrogen bond networks: 1) the $\delta 1$ -oxygen atom of N38 on strand- $\beta 3$
230 in the N-terminal domain bonds with the backbone nitrogen atom of G95 on the loop

231 connecting strand- β 6 with strand- β 7; 2) the δ 2 –oxygen atom of D39 on strand- β 3
232 bonds with the γ 1 –oxygen atom of T48 on the loop connecting strand- β 3 with helix- α 2
233 in the middle domain of another protomer; 3) the nitrogen atom of δ 2 –N157 on the turn
234 connecting strand- β 10 with strand- β 11 stacks against the γ 1 –oxygen atom of T278 on
235 β 14; and 4) the η –oxygen atom of Y58 on helix- α 2 stacks against ϵ 2 –oxygen atom of
236 E263 on strand- β 13 in the C-terminal domain (Fig. 5). Within the interface of the two
237 trimers, L2 and E3 on helix- α 1 as well as V26 on strand- β 1 of protomer B pack face to
238 face against E3 and L2 on helix- α 1 as well as N52 on helix- α 2 of its counterpart protomer
239 A, respectively. Moreover, the N-terminus of subunit C is close to monomer A, with the
240 closest atom-to-atom distance being 3.2 Å between residues A112 in protomer C and
241 N110 in protomer A, suggesting that this close proximity may assist in the hexamer
242 assembly process (Fig. 5).

243 To validate the significance of the interfaces, analytical ultracentrifugation (AUC)
244 analysis was conducted to assess the oligomeric form of soluble and stable variants.
245 Mutant D39A primarily existed as a hexamer, while mutant E263A distributed equally
246 between the monomer and hexamer states. By comparison, mutants N38A, Y58A and
247 N157A existed predominately as monomers (Fig. 6A). DSF assays revealed that the
248 denaturation profiles of the hexameric proteins (wild type and D39A Nsp15) indicated a
249 melting temperature (T_m) of 46 °C. E263A denatured at 43 °C, while the T_m shifted to
250 approximately 37-38 °C for the monomeric mutants N38A, N157A and Y58A (Fig. 6B).
251 Taken together, we inferred that the hexameric form rendered the protein more stable and
252 may thus impact protein function.

253 In an effort to evaluate the functional state and demonstrate how oligomeric assembly

254 affects NendoU activity, the RNA binding ability and the NendoU activity of these
255 variants were further assessed. The results of the FP and FRET-based assays showed that
256 the hexameric mutant D39A bound to RNA R1 with a binding affinity (626.22
257 ± 24.80 nM) higher than that of the wild-type protein, which may explain why mutant
258 D39A exhibited greater enzymatic activity than the wild-type Nsp15. Mutant E263A,
259 which displayed an equal distribution between the monomer and hexamer states, retained
260 an impaired binding affinity (1013.43 ± 77.38 nM), matching its moderately inhibited
261 activity. Consistently, associations between the monomeric variants (N38A, Y58A and
262 N157A) and RNA R1 were barely detectable, and the activities of the monomeric mutants
263 were abolished (Fig. 6C-D). Altogether, the correlation between RNA binding
264 affinity and NendoU activity showed that RNA binds only to the hexameric state,
265 indicating that oligomeric assembly may regulate NendoU activity by impacting its RNA
266 binding ability (Table 3).

267

268 **Effects of Mn^{2+} and Mg^{2+} on MERS-Nsp15**

269 We further investigated the effect of Mn^{2+} on the activity of MERS-Nsp15. A significant
270 increase in activity was observed as the concentration of Mn^{2+} was increased from 0 to 15
271 mM, with a 3-fold increase in activity under 10 mM Mn^{2+} (Fig. 7A). Fluorescence
272 polarization (FP) assays were then conducted to examine the Nsp15-RNA binding
273 affinity with increasing Mn^{2+} concentration. The Nsp15-RNA binding affinity increased
274 with the addition of Mn^{2+} , revealing that the function of Mn^{2+} may be a result of the
275 increasing substrate binding ability of Nsp15 (Fig. 7B).

276 To determine whether Mg^{2+} can also affect the activity of MERS-Nsp15, we performed
277 FRET-based assays and FP assays in which Mg^{2+} concentrations were increased. The
278 catalytic activity of Nsp15 increased slightly in the presence of 15 mM Mg^{2+} (Fig. 7C).
279 Consistently, the Nsp15-RNA binding ability was similar in the presence or absence of
280 Mg^{2+} (Fig. 7D), indicating that the effect of Mg^{2+} *in vitro* was minor compared to the
281 effect of Mn^{2+} .

282

283 **Effects of CoV RTC-associated protein Nsp8 and the Nsp7/Nsp8 complex on Nsp15**

284 In agreement with previous evidence that MHV Nsp15 strongly colocalizes with primase
285 Nsp8 as well as polymerase Nsp12, immunoprecipitation (IP) experiments also
286 confirmed the binding of MHV Nsp15 to MHV Nsp12 as well as to MHV Nsp8 (20).
287 Pull-down assays were further performed, and the direct interaction between Nsp15 and
288 Nsp8 was monitored, but it was not monitored between Nsp15 and Nsp12 (Fig. 8A). To
289 ascertain whether the interaction between Nsp15 and Nsp8 is dependent on the hexameric
290 state of Nsp15, his-tagged Nsp8 was copurified with the flag-tagged Nsp15 mutants
291 (N38A, D39A, E263A and N157A) harboring distinct oligomeric states and detected by
292 pull-down assays. Nsp8 was shown to interact with each of the Nsp15 variants, indicating
293 that both monomeric Nsp15 and hexameric Nsp15 interact with Nsp8 (Fig. 8A).

294 Nsp8 was cocrystallized with Nsp7 as a hexadecameric complex that displayed
295 primase-like RdRp activity and dramatically increased the polymerase activity of Nsp12
296 (23, 25). We therefore examined whether Nsp15 binds to Nsp8 in the context of an
297 Nsp7/Nsp8 complex and affects the endoribonuclease activity of Nsp15. To obtain the
298 Nsp7/Nsp8 complex, purified Nsp7 and Nsp8 were incubated in a 1:1 molar ratio, and the

299 elution peak representing the Nsp7/Nsp8 complex was isolated via gel filtration and
300 corroborated by SDS-PAGE. We next detected and quantified the interaction of Nsp15
301 with Nsp8 and the Nsp7/Nsp8 complex by microscale thermophoresis (MST) assay, a
302 sensitive method that can be used to monitor and quantify binding affinities of complex
303 formation between proteins (24). MST results revealed binding between Nsp15 and Nsp8
304 with a K_d value of $16.33 \pm 3.21 \mu\text{M}$ (Fig. 8B). Notably, relatively enhanced affinity
305 ($6.48 \pm 1.47 \mu\text{M}$) was observed for the Nsp7/Nsp8 complex titrated with fluorescently
306 labeled Nsp15 (Fig. 8C). As a control, Nsp7 alone displayed no binding to Nsp15 by
307 MST (Fig. 8C). However, we have been unable to detect binding between Nsp12 and the
308 fluorescently labeled Nsp15 by the MST assay (Fig. 8B).

309 To test whether Nsp8 or Nsp7/Nsp8 impact the NendoU activity of Nsp15, we
310 preincubated Nsp15 with Nsp8 and the Nsp7/Nsp8 complex at a 1:1 molar ratio before
311 performing the FRET-based assays. The catalytic rate increased from $1.25 \pm 0.06 \text{ nM s}^{-1}$
312 to $1.88 \pm 0.09 \text{ nM s}^{-1}$ in the presence of Nsp8, while the Nsp7/Nsp8 complex increased
313 the NendoU activity to $1.89 \pm 0.04 \text{ nM s}^{-1}$ (Fig. 8D). To further demonstrate whether this
314 enzymatic enhancement is related to the oligomeric state of Nsp15, we measured the
315 catalytic rate of the variants D39A, E263A and N157A in the presence of Nsp8 or the
316 Nsp7/Nsp8 complex. Nsp8 enhanced the catalytic rate of the hexameric D39A protein by
317 58 %, while the Nsp7/Nsp8 complex increased the catalytic rate by 54 % (Fig. 8E). For
318 E263A, the activity increased by 33 % in the presence of Nsp8 and increased by 40 % in
319 the presence of Nsp7/Nsp8 (Fig. 8E). However, the activity of the monomeric N157A
320 protein was similar in the presence of Nsp8 or Nsp7/Nsp8, demonstrating that this
321 enhancement effect is highly dependent on the hexameric state of Nsp15.

322

323

324 **DISCUSSION**

325 In this study, we described the crystal structure of MERS-Nsp15 refined to a 2.7 Å
326 resolution. Structural examination of the active site and subunit interaction surfaces,
327 together with biochemical characterization of the critical mutants, revealed that NendoU
328 activity was mediated by 1) catalytic residues within the active site pocket that were
329 indispensable for NendoU activity; 2) residues directly interacting with RNA; and 3)
330 residues providing structural support for hexameric assembly, which is the functionally
331 active state that is responsible for its RNA binding ability.

332 Notably, several different features were identified in MERS-Nsp15 compared to its
333 homologs. For example, the endoribonuclease activity of the variant F285A was slightly
334 increased and the activity of F285S increased about 31% compared to that of the
335 wild-type protein. Examination of the neighboring structure shows that substitution of
336 F285 with alanine or serine likely offsets the steric obstruction of the aromatic side chain,
337 which may spatially interfere with substrate binding in the pocket, and thus, likely widens
338 the active site cavity and facilitates access to the substrate. FP assays confirmed that
339 F285A and F285S displayed increased binding affinity for RNA. In particular, the effect
340 of serine substitution on activity enhancement was more dramatic than that of alanine
341 substitution, possibly due to the fact that serine is hydrophilic, whereas alanine is
342 hydrophobic. More importantly, sequence alignment demonstrated that at the equivalent
343 position of F285, a serine is conserved among other coronaviruses as well as most
344 arteriviruses, and an alanine is present at the equivalent position in EAV (equine arteritis
345 virus) (Fig. 4). Thus, considering that MERS-Nsp15 is the only exception, it is plausible

346 that F285 may exist in MERS-Nsp15 to mediate the function of this protein.

347 Another example is the hexameric mutant D39A, which exhibited higher activity than the
348 wild-type protein. The corresponding mutant D39A from SARS-Nsp15 primarily existed
349 as a monomer and displayed no activity (14). It is likely that apart from interacting with
350 T48, D39 from SARS-Nsp15 also forms an ionic bond with R90, which contributes more
351 to the interprotomer interactions and may explain why mutant D39A exists in different
352 oligomeric states in SARS-Nsp15 and MERS-Nsp15. Remarkably, mutant D39A from
353 MERS-Nsp15 exhibited a higher RNA binding affinity compared to wild-type protein,
354 which may explain its higher activity.

355 Previous studies have demonstrated that the activity of Nsp15 from both SARS-CoV and
356 MHV can be stimulated by Mn^{2+} (11-14). The activity of MERS-Nsp15 increased with
357 the addition of Mn^{2+} , with enhanced RNA binding affinity (Fig. 7A-B). However, Mg^{2+}
358 only slightly enhanced NendoU activity and did not influence RNA binding (Fig. 7C-D).
359 It is plausible that NendoU activity could be regulated by RNA binding via Mn^{2+} . In
360 contrast, structures of MERS-Nsp15 and its orthologs all show no obvious metal binding
361 sites, arguing against the direct involvement of Mn^{2+} . We speculate that Mn^{2+} may serve
362 as a cofactor to stabilize the RNA-Nsp15 structure and thus enhance NendoU activity.
363 Moreover, given that the intracellular concentration of these divalent metal ions is
364 estimated to be within the micromolar range, these biochemical observations from *in*
365 *vitro* studies may not be applicable to the *in vivo* environment. Taken together, more
366 information is needed to elucidate the roles that Mn^{2+} and Mg^{2+} play in the catalytic
367 process and the possible mechanism.

368 If the hexamer assembles in such a way that three monomers first constitute a trimer and
369 two trimers pack back-to-back into a hexamer as proposed, then the trimer state should be

370 possible. Nonetheless, the trimer could not be isolated and biochemically characterized in
371 our work nor in previous studies, as the mutation of any of these residues (L2, E3, V26,
372 N52 and N110), which are located at the preconceived trimer-trimer interfaces, only
373 yielded proteins that were predominantly monomeric in solution (14). One possible
374 explanation of this discrepancy may be that the trimer is highly unstable and is transient
375 in nature.

376 Nsp15 interacted with Nsp8 during both the pull-down and MST assays. Remarkably,
377 Nsp15 binds to the Nsp7/Nsp8 complex with a stronger binding affinity compared to
378 Nsp8. In contrast to previous IP results (20), both the pull-down and MST assays could
379 not detect an interaction between Nsp15 and Nsp12, possibly due to the extremely weak
380 interaction. Moreover, given that Nsp12 can complex with Nsp8 and Nsp7 (20), another
381 possible explanation might be that the detected interaction between Nsp12 and Nsp15 by
382 IP was a result from the indirect binding of Nsp12 with Nsp8 instead of the direct binding
383 with Nsp15.

384 In addition, NendoU activity may be increased by both Nsp8 and the Nsp7/Nsp8
385 complex, with this increase only being observed for the hexameric state of Nsp15, further
386 strengthening the hypothesis that the hexameric state is the functional form. However, the
387 mechanism through which NendoU activity is enhanced by Nsp8 and the Nsp7/Nsp8
388 complex remains unclear. It is likely that the interaction between Nsp8 and Nsp15 may
389 provide a possible explanation (*ie.*, the direct interaction might induce a conformational
390 change in Nsp15). Indeed, the SARS-CoV Nsp7/Nsp8 complex may bind RNA and has
391 been shown to confer RNA binding ability to SARS-CoV Nsp12 (23, 25). We speculate,
392 therefore, that Nsp8 or the Nsp7/Nsp8 complex may increase NendoU activity by
393 enhancing the RNA binding ability of Nsp15. Further studies are required to elucidate

394 mechanisms for the involvement of Nsp15 in the Nsp7/Nsp8/Nsp15 complex and the role
395 Nsp15 may play in viral replication/transcription complex machinery and coronavirus
396 pathogenesis.

397 In conclusion, we provide the first structure of MERS-Nsp15, and our structure-function
398 studies demonstrate crucial features and provide important novel insights into how
399 NendoU activity is possibly mediated. Moreover, given that inhibitors targeting the
400 catalytic sites may potentially interfere with endoribonuclease within host cells, this work
401 also provides new insights on how drugs designed to disrupt interprotomer interaction
402 surfaces may be applied.

403

404

405 **MATERIALS AND METHODS**

406 **Construct design and molecular cloning.** The sequence encoding the MERS-Nsp15
407 protein was optimized for expression in *E. coli* and was synthesized by Genscript. A
408 hexahistidine tag was inserted at the N-terminal end via PCR with the forward primer
409 (5'-CATGCCATGGGCCACCACCACCACCACCACGGCCTGGAAAACATTGCGTTT
410 AATG-3') and the reverse primer
411 (5'-CCGCTCGAGTTATTGCAGGCGCGGATAGAAGGTTTGAC-3'). The PCR
412 product was then cloned into the pRSF-Duet1 vector between the *NcoI* and *XhoI* sites.
413 Point mutations were introduced into the wild-type Nsp15 plasmid using the Fast
414 Mutagenesis System (Transgene Biotech). Nsp15 and Nsp15 mutants (N38A, D39A,
415 N157A and E263A) possessing a flag tag at the N-terminus were constructed in a similar
416 procedure.

417

418 **Expression and purification of MERS-Nsp15.** The sequence-verified MERS-Nsp15
419 plasmid was transformed into *E. coli* strain BL21 (DE3) cells. The cells were cultured in
420 LB medium containing kanamycin (100 mg liter⁻¹) until the optical density (OD_{600nm})
421 reached 0.6-0.8. The cell culture was then cooled to 16 °C and induced with 0.4 mM
422 isopropyl- β -D-1-thiogalactopyranoside (IPTG). After 14-16 hours of induction, the cells
423 were harvested and lysed in buffer containing 50 mM Tris-HCl, pH 8.0, 150 mM NaCl
424 and 70 mM imidazole. The lysate was centrifuged at 25,000 \times g for 40 min, and the
425 soluble supernatant was purified by immobilized metal ion affinity chromatography. The
426 eluate was fractionated via a Superdex-200 10/300 (GE Healthcare) column with buffer
427 containing 10 mM Tris-HCl, pH 7.5, and 50 mM NaCl. The protein was concentrated to 8
428 mg/ml for crystal screening or stored at -80 °C for further use. The MERS-Nsp15
429 mutants described in this paper were expressed and purified following a similar protocol
430 as described above.

431 Recombinant MERS-CoV Nsp8 containing both GST and hexahistidine tags and
432 MERS-CoV Nsp7 with a GST tag were expressed and purified as previously reported for
433 SARS-CoV Nsp7 and Nsp8 (25). To obtain Nsp7/Nsp8 complex, purified Nsp7 and Nsp8
434 were incubated in a 1:1 molar ratio at 4°C for 1 hour and then the proteins were separated
435 by Superdex-200 10/300 column. The elution peak representing Nsp7/Nsp8 complex was
436 further corroborated by SDS-PAGE, and the oligomeric state was evaluated by analytical
437 ultracentrifugation (AUC) analysis. MERS-CoV Nsp12 carrying both the N-terminal
438 GST tag and the C-terminal hexahistidine tag was expressed in the baculovirus

439 expression system (Bac-to-Bac system, Invitrogen) with the Sf9 insect cell line. The
440 GST-fused Nsp12 was primarily purified via a glutathione affinity column and was then
441 digested by thrombin protease overnight to release the GST tag. Then, Nsp12 was further
442 purified using a Hitrap Q (GE Healthcare) column and a Superdex-200 10/300 column
443 (GE Healthcare) to over 95% purity.

444

445 **Crystallization and structure determination.** MERS-Nsp15 crystals were grown at 289
446 K by the hanging drop vapor diffusion method. Crystals were grown overnight in a
447 mixture of 1 μ l protein and 1 μ l reservoir solution (4 % v/v tacsimate, pH 4.0, and 12 %
448 w/v polyethylene glycol 3350). Crystals were transferred to a cryoprotected buffer
449 (reservoir solution and 25 % glycerol) and flash frozen in liquid nitrogen.

450 The data set for Nsp15 was collected at BL19 beamline in the Shanghai Synchrotron
451 Radiation Facility (SSRF), and the data were processed and scaled using the XDS
452 program suite (26). The native Nsp15 structure was solved by molecular replacement
453 with the program Phaser of the CCP4 using MHV Nsp15 (PDB code: 2GTH) as the
454 search model, and the structure refinement was carried out with PHENIX (12, 27-29).
455 Final refinement statistics are summarized in Table 1. Structural figures were drawn with
456 PyMOL (30).

457

458 **Analytical ultracentrifugation analysis.** Purified MERS-Nsp15 and mutant proteins
459 were subjected to analytical ultracentrifugation (AUC) analysis in a buffer containing 20
460 mM Tris, pH 7.5, and 50 mM NaCl. Sedimentation rate experiments were conducted at 4
461 °C in a proteomeLab XL-1 Protein Characterization System (Beckman Coulter). The data

462 were collected at 45,000 rpm using an An-60 Ti rotor (Beckman Coulter) and processed
463 according to a c (S) distribution model.

464

465 **Differential scanning fluorimetry assay.** A differential scanning fluorimetry (DSF)
466 assay was carried out in a real-time PCR machine (LightCycler480II). Each 20- μ l
467 reaction mixture contained 0.5 mg/ml purified protein. SYPRO orange was diluted to a
468 5 \times final concentration. The temperature was held for 10s and increased from 25 $^{\circ}$ C to 95
469 $^{\circ}$ C at a rate of 1 $^{\circ}$ C/min. The average fluorescence intensity and melting temperature
470 (T_m) of three measurements were determined and used.

471

472 **RNA oligonucleotides synthesis.** RNA oligonucleotides (R1-R3) were synthesized and
473 purified by Genewiz to over 95% purity. RNA R1 contains 20 rU
474 (5'-rUrUrUrUrUrUrUrUrUrUrUrUrUrUrUrUrUrU-3'). RNA R2
475 (5'-rUrUrArArCrGrArArCrU-3') is derived from the conserved sequence of the
476 transcriptional regulatory sequence (TRS) of the MERS-CoV genome, and RNA R3 is a
477 double-stranded RNA annealed by R2 and its complementary strand
478 (5'-rArGrUrUrCrGrUrUrArA-3').

479

480 **Fluorescence polarization assay.** RNA oligonucleotides used for the fluorescence
481 polarization (FP) assays were labeled at the 3' end with Cy3 and diluted to a final
482 concentration of 100 nM. Purified Nsp15 was diluted with buffer containing 20 mM Tris,
483 pH 7.5, and 50 mM NaCl. The effects of divalent ions were detected in the presence of 0
484 mM, 2mM, 5 mM, 10 mM or 15 mM $MnCl_2$ or $MgCl_2$. Reaction mixtures with a total

485 volume of 100 μ l were prepared, and FP assays were performed using a Perkin-Elmer
486 Envision with the excitation wavelength of 555 nm and the emission wavelength of 595
487 nm. All Nsp15 proteins used for the FP assays in this paper harbored the K286A mutation
488 that abolishes NendoU activity to avoid substrate digestion. The anisotropy values
489 reported were the average of three replicates, and the means \pm SD results were shown.
490 Data were further analyzed in Origin 8.0 (OriginLab) using the Hill equation. The
491 calculated dissociation constant (Kd) and the Hill coefficient are listed in Table 2.

492

493 **Endoribonuclease assay.** Real-time endoribonuclease assays were performed using
494 fluorescent resonance energy transfer (FRET) as described previously (12). Substrate
495 (5'-6-FAM-dArUdAdA-6-TAMRA-3') was purchased from TAKARA. The substrate had
496 a carboxyfluorescein (FAM) at the 5' end and a tetramethylrhodamine (TAMRA) at the 3'
497 end, which quenches the FAM fluorescent emission at 518 nm. The cleavage of the
498 substrate leads to increasing fluorescence emission at 518 nm. The cleavage reaction was
499 performed at room temperature and contained 0.2 μ M protein and 1.2 μ M RNA substrate
500 in a final volume of 100 μ l. The fluorescence intensity over time was monitored by the
501 EnSpire Multimode Plate Reader system (PerkinElmer) with the excitation wavelength of
502 498 nm and the emission wavelength of 518 nm.

503 The endoribonuclease assays of wild-type Nsp15 and its mutants were performed in
504 buffer containing 50 mM Tris, pH 7.5, and 50 mM KCl. Nsp8, the Nsp7/Nsp8 complex,
505 Nsp12 and the spike protein (spike protein of MERS-CoV) were adjusted to a 1:1 molar
506 ratio with Nsp15 at a final concentration of 0.2 μ M. Nsp15 was preincubated with Nsp8,
507 Nsp7/Nsp8 complex, Nsp12 and S protein for 30 min, respectively, before RNA substrate

508 was introduced. Wild-type Nsp15 and mutants D39A, E263A and N157A were
509 preincubated with 0.2 μ M Nsp8 or 0.2 μ M Nsp7/Nsp8 complex, respectively. The effects
510 of divalent ions were detected in the presence of 0 mM, 2mM, 5 mM, 10 mM or 15 mM
511 $MnCl_2$ or $MgCl_2$. The enzymatic activity data were analyzed in Origin 8.0 (OriginLab).
512 All assays were repeated three times, and the means \pm SD results were shown in this
513 paper.

514

515 **Binding affinity quantifications by microscale thermophoresis.** Binding affinity was
516 detected by microscale thermophoresis (MST) using Monolith NT.115 (Nanotemper
517 Technologies) as previously reported (24). Purified MERS-Nsp15 was labeled and
518 centrifuged at 14000 rpm for 10 min to eliminate precipitates. A serial dilution of
519 recombinant Nsp7, Nsp8, Nsp12 and the Nsp7/Nsp8 complex was applied within buffer
520 containing 20 mM Tris, pH 7.0, 50 mM NaCl and 0.05% Tween-20. Affinity
521 measurements were conducted in hydrophilic capillaries (Nanotemper, K002 MonolithTM
522 NT.115 Hydrophobic Capillaries). Each measurement was repeated at least three times.
523 The sigmoidal curves were normalized with the mean \pm SD of each data point, and Kd
524 values were calculated.

525

526 **Pull-down and western blot.** Purified flag-tagged Nsp15 was incubated with his-tagged
527 Nsp8, his-tagged Nsp8/Nsp7 (Nsp7 has no tag) complex and his-tagged Nsp12 at 4 °C
528 overnight and then applied to anti-flag beads. Nsp15 mutants N38A, D39A, N157A and
529 E263A were bound to anti-flag beads and incubated with his-tagged Nsp8, with
530 his-tagged Nsp12 or without protein. Beads were washed with PBS buffer and

531 resuspended in electrophoresis sample buffer for SDS-PAGE. Polyacrylamide gel was
532 transferred to polyvinylidene difluoride (PVDF) membranes and blocked by 5 % milk in
533 TBST buffer. Anti-his antibodies were applied for 1 hour at room temperature and then
534 washed with TBST buffer. After incubation with the second antibody, blots were washed,
535 detected and documented on X-ray film.

536

537 **Accession number.** The coordinates and structure factors for MERS-Nsp15 have been
538 deposited in the Protein Data Bank (PDB) under the accession code 5YVD.

539

540

541 **ACKNOWLEDGMENTS**

542 We are grateful to the staff at the Shanghai Synchrotron Radiation Facility (China) for
543 their assistance with X-ray diffraction data collection. This work is supported by the
544 National Major Project Grants 2017YFC0840300 and the National Natural Science
545 Foundation of China (81330036, 31570717, 81621005, and 81520108019).

546

547

548 **REFERENCES**

- 549 1. Hilgenfeld R, Peiris M. 2013. From SARS to MERS: 10 years of research on highly
550 pathogenic human coronaviruses. *Antiviral Research* 100:286-95.
- 551 2. Fehr AR, Channappanavar R, Perlman S. 2016. Middle East Respiratory Syndrome:
552 Emergence of a Pathogenic Human Coronavirus. *Annual Review of Medicine* 68.

- 553 3. Cavanagh D. 1997. Nidovirales: a new order comprising Coronaviridae and
554 Arteriviridae. *Archives of Virology* 142:629-633.
- 555 4. Sawicki SG, Sawicki DL. 1995. Coronaviruses use discontinuous extension for
556 synthesis of subgenome-length negative strands. *Oxygen Transport to Tissue*
557 XXXIII 380:499-506.
- 558 5. Prentice E, McAuliffe J, Lu X, Subbarao K, Denison MR. 2004. Identification and
559 characterization of severe acute respiratory syndrome coronavirus replicase proteins.
560 *Journal of Virology* 78:9977.
- 561 6. Gao F, Ou HY, Chen LL, Zheng WX, Zhang CT. 2003. Prediction of proteinase
562 cleavage sites in polyproteins of coronaviruses and its applications in analyzing
563 SARS-CoV genomes. *Febs Letters* 553:451-456.
- 564 7. Pasternak AO, Spaan WJ, Snijder EJ. 2006. Nidovirus transcription: how to make
565 sense...? *Journal of General Virology* 87:1403-1421.
- 566 8. Sawicki SG, Sawicki DL. 2005. Coronavirus Transcription: A Perspective. *Current*
567 *Topics in Microbiology & Immunology* 287:31.
- 568 9. Ivanov KA, Hertzog T, Rozanov M, Bayer S, Thiel V, Gorbalenya AE, Ziebuhr J.
569 2004. Major genetic marker of nidoviruses encodes a replicative endoribonuclease.
570 *Proceedings of the National Academy of Sciences of the United States of America*
571 101:12694.
- 572 10. Bhardwaj K, Palaninathan S, Alcantara JM, Yi LL, Guarino L, Sacchettini JC, Kao
573 CC. 2008. Structural and functional analyses of the severe acute respiratory

- 574 syndrome coronavirus endoribonuclease Nsp15. *Journal of Biological Chemistry*
575 283:3655.
- 576 11. Bhardwaj K, Guarino L, Kao CC. 2004. The severe acute respiratory syndrome
577 coronavirus Nsp15 protein is an endoribonuclease that prefers manganese as a
578 cofactor. *Journal of Virology* 78:12218.
- 579 12. Xu X, Zhai Y, Sun F, Lou Z, Su D, Xu Y, Zhang R, Joachimiak A, Zhang XC,
580 Bartlam M. 2006. New antiviral target revealed by the hexameric structure of mouse
581 hepatitis virus nonstructural protein nsp15. *Journal of Virology* 80:7909-17.
- 582 13. Ricagno S, Egloff MP, Ulferts R, Coutard B, Nurizzo D, Campanacci V, Cambillau
583 C, Ziebuhr J, Canard B. 2006. Crystal structure and mechanistic determinants of
584 SARS coronavirus nonstructural protein 15 define an endoribonuclease family.
585 *Proceedings of the National Academy of Sciences of the United States of America*
586 103:11892-11897.
- 587 14. Bhardwaj K, Palaninathan S, Alcantara JM, Yi LL, Guarino L, Sacchettini JC, Kao
588 CC. 2008. Structural and functional analyses of the severe acute respiratory
589 syndrome coronavirus endoribonuclease Nsp15. *Journal of Biological Chemistry*
590 283:3655.
- 591 15. Joseph JS, Saikatendu KS, Subramanian V, Neuman BW, Buchmeier MJ, Stevens
592 RC, Kuhn P. 2007. Crystal Structure of a Monomeric Form of Severe Acute
593 Respiratory Syndrome Coronavirus Endonuclease nsp15 Suggests a Role for
594 Hexamerization as an Allosteric Switch. *Journal of Virology* 81:6700-8.

- 595 16. Kang H, Bhardwaj K, Li Y, Palaninathan S, Sacchettini J, Guarino L, Leibowitz JL,
596 Kao CC. 2007. Biochemical and genetic analyses of murine hepatitis virus Nsp15
597 endoribonuclease. *Journal of Virology* 81:13587-13597.
- 598 17. Lei Y, Moore CB, Liesman RM, O'Connor BP, Bergstralh DT, Chen ZJ, Pickles RJ,
599 Ting JPY. 2009. MAVS-Mediated Apoptosis and Its Inhibition by Viral Proteins.
600 *Plos One* 4:e5466.
- 601 18. Bhardwaj K, Liu P, Leibowitz JL, Kao CC. 2012. The Coronavirus
602 Endoribonuclease Nsp15 Interacts with Retinoblastoma Tumor Suppressor Protein.
603 *Journal of Virology* 86:4294.
- 604 19. Deng X, Hackbart M, Mettelman RC, O'Brien A, Mielech AM, Yi G, Kao CC,
605 Baker SC. 2017. Coronavirus nonstructural protein 15 mediates evasion of dsRNA
606 sensors and limits apoptosis in macrophages. *Proceedings of the National Academy*
607 *of Sciences of the United States of America* 114:E4251.
- 608 20. Athmer J, Fehr AR, Grunewald M, Smith EC, Denison MR, Perlman S. 2017. *In*
609 *Situ* Tagged nsp15 Reveals Interactions with Coronavirus Replication/Transcription
610 Complex-Associated Proteins. *Mbio* 8:e02320-16.
- 611 21. Posthuma CC, Nedialkova DD, Zevenhoven-Dobbe JC, Blokhuis JH, Gorbalenya
612 AE, Snijder EJ. 2006. Site-directed mutagenesis of the Nidovirus replicative
613 endoribonuclease NendoU exerts pleiotropic effects on the arterivirus life cycle.
614 *Journal of Virology* 80:1653-1661.

- 615 22. Hoover HS, Wang CY, Middleton S, Ni P, Zlotnick A, Vaughan RC, Kao CC. 2016.
616 Phosphorylation of the Brome Mosaic Virus Capsid Regulates the Timing of Viral
617 Infection. *Journal of Virology* 90:7748.
- 618 23. Subissi L, Posthuma CC, Collet A, Zevenhoven-Dobbe JC, Gorbalenya AE, Decroly
619 E, Snijder EJ, Canard B, Imbert I. 2014. One severe acute respiratory syndrome
620 coronavirus protein complex integrates processive RNA polymerase and
621 exonuclease activities. *Proceedings of the National Academy of Sciences of the*
622 *United States of America* 111:3900-9.
- 623 24. Seidel SAI, Dijkman PM, Lea WA, Bogaart GVD, Jerabek-Willemsen M, Lazic A,
624 Joseph JS, Srinivasan P, Baaske P, Simeonov A. 2013. Microscale thermophoresis
625 quantifies biomolecular interactions under previously challenging conditions.
626 *Methods* 59:301-315.
- 627 25. Zhai Y, Sun F, Li X, Pang H, Xu X, Bartlam M, Rao Z. 2005. Insights into
628 SARS-CoV transcription and replication from the structure of the nsp7–nsp8
629 hexadecamer. *Nature Structural & Molecular Biology* 12:980.
- 630 26. Kabsch W. 2010. XDS. *Acta Crystallogr D Biol Crystallogr* 66:125–132.
- 631 27. McCoy AJ, Grosse-Kunstleve RW, Adams PD, Winn MD, Storoni LC, Read RJ. 2007.
632 Phaser crystallographic software. *Journal of Applied Crystallography* 40:658-674.
- 633 28. Potterton E, McNicholas S, Krissinel E, Cowtan K, Noble M. 2010. The CCP4
634 molecular-graphics project. *Acta Crystallogr D Biol Crystallogr* 58:1955-1957.

- 635 29. Sauter NK. 2010. PHENIX: building new software for automated crystallographic
636 structure determination. *Acta Crystallographica* 58:1948-1954.
- 637 30. Delano WL. 2002. The PyMOL Molecular Graphics System (2002). *My*
638 *Publications* 30:442-454.
- 639 31. Thompson JD, Higgins DG, Gibson TJ. 1994. CLUSTAL W: improving the
640 sensitivity of progressive multiple sequence alignment through sequence weighting,
641 position-specific gap penalties and weight matrix choice. *Nucleic Acids Res*,
642 22:4673– 4680.
- 643 32. Gouet P, Jones JD, Hoffman NE, Nussaume L. ESPript: analysis of multiple
644 sequence alignments in PostScript. *Bioinformatics*, 15:305–308.

645
646
647 **FIGURE LEGENDS**

648 **FIG 1 Overall structure of MERS-Nsp15.** (A) Cartoon representation and schematic
649 diagram of the overall structure of a protomer. A schematic diagram of the domain
650 boundaries in the amino-acid sequence is shown above the cartoon. The N-terminal
651 domain, middle domain and C-terminal domain are colored red, green and blue,
652 respectively. The surface transparency is set to 20 %. (B) Side view of the cartoon
653 representation of the hexamer. Three protomers within a trimer are colored green, yellow
654 and blue, with the other trimer colored gray. (C) Side view and top view of the
655 distribution of the N-terminal domain, middle domain and C-terminal domain within the

656 hexamer by surface representation. Six protomers are colored differently. The N-terminal
657 domain, middle domain and C-terminal domain within one protomer are colored red,
658 green and blue and are labeled N, M and C, respectively. Six protomers form a hexamer
659 through the N- to N-terminal interaction.

660

661 **FIG 2 Comparison of MERS-Nsp15 with SARS-Nsp15 and MHV Nsp15.** (A) The
662 structures of MERS-Nsp15, SARS-Nsp15 (PDB code: 2H85) and MHV (PDB code:
663 2GTH) Nsp15 are superposed together. Monomers and trimers are shown separately, and
664 r.m.s.d. of C α atoms are listed. (B) Three domains of the monomer for MERS-Nsp15,
665 SARS-Nsp15 and MHV Nsp15 are aligned, and r.m.s.d. of C α atoms are listed.

666

667 **FIG 3 Sequence alignment of MERS-Nsp15 with coronaviruses and arteriviruses.**
668 Key residues within the catalytic center are marked by red arrowheads and residues in the
669 subunit interfaces are marked by blue circles. Strictly conserved residues are depicted in
670 white characters on a black background. Secondary structure elements are shown on top
671 of the alignment (helices are represented by squiggles, β -strands by arrows and turns by
672 the letters TT). Sequences are aligned using ClustalW (31), and the figure is drawn by
673 ESPript (32). NCBI accession numbers are as follow: YP_009047226 for Middle East
674 respiratory syndrome-related coronavirus (MERS-CoV); AGT21317 for SARS
675 coronavirus (SARS-CoV); NP_740619 for murine hepatitis virus strain A59 (MHV);
676 AGT21366 for human coronavirus 229E (HCoV-229E); AIM47753 for porcine epidemic
677 diarrhea virus (PEDV); AGZ84515 for feline infectious peritonitis virus (FIPV);

678 ABG89333 for transmissible gastroenteritis virus virulent Purdue (TGEV); and
679 NP_705592 for equine arteritis virus (EAV).

680

681 **FIG 4 Identification and characterization of residues within the catalytic center of**

682 **MERS-Nsp15.** (A) Structural superposition of MERS-Nsp15 and SARS-Nsp15 (PDB

683 code: 2H85) (13). The structure of MERS-Nsp15 is colored magenta, and the structure of

684 SARS-Nsp15 is colored yellow. The catalytic center of MERS-Nsp15 superimposed with

685 SARS-Nsp15 is enlarged in panel A (the cartoon transparency is set to 20 %). Residues

686 discussed in this paper are labeled with stick representations (magenta, MERS-Nsp15;

687 yellow, SARS-CoV Nsp15). Equivalent residues located in the catalytic site of

688 SARS-Nsp15 are listed below. (B) Protein-RNA binding profiles and the inhibitory

689 effects of the cleavage of the fluorescent substrate by RNA R1, R2 and R3. R1 contains

690 20 rU and exhibits a K_d value of 818.28 ± 50.39 nM. R2 binds to Nsp15 with a K_d

691 value of 1190.52 ± 137.91 nM. R3 exhibits a K_d value of 932.49 ± 49.40 nM. The

692 activity of the wild-type Nsp15 in the absence of R1, R2 or R3 is set to 100%.

693 Fluorescent intensity is measured at each RNA (R1-R3) concentration, and the values

694 shown are the average of three measurements. (C) DSF profile of wild-type Nsp15. All

695 mutants listed in panel A share similar melting temperatures and DSF profiles as

696 wild-type Nsp15. (D) NendoU activity profile for the mutants with alanine substitution of

697 residues located within the catalytic site. FRET-based assays for different mutants are

698 conducted, and the reaction rate is calculated. (E) NendoU activity profile for active-site

699 mutants with alanine substitutions and the corresponding residue in SARS-Nsp15.

700

701 **FIG 5 Stick representation of residues involved in the interprotomer interaction of**
702 **MERS-Nsp15.** A side view of the surface representation of the interactions within three
703 protomers is shown. Protomers A, B and C are colored blue, yellow and magenta,
704 respectively. Residues involved in the subunits interaction are labeled with stick
705 representations (blue, subunit A; yellow, subunit B; and magenta, subunit C; the cartoon
706 transparency is set to 20 %). Four contact regions are boxed and enlarged. The atomic
707 distances are measured by PyMOL.

708

709 **FIG 6 Biochemical characterization of mutants critical for the oligomeric assembly**
710 **of MERS-Nsp15.** (A) Analytical ultracentrifuge (AUC) analysis of mutants containing
711 mutations located at interaction surfaces. AUC profiles of wild-type protein, D39A,
712 E263A, N38A, Y58A and N157A mutants are shown. The first peak at approximately 40
713 kD represents the position of the monomer, and the second peak at approximately 240 kD
714 represents the position of the hexamer. (B) DSF profiles of wild-type Nsp15 and mutants
715 D39A, E263A, N38A, Y58A and N157A. (C) Protein-RNA binding profiles of the Nsp15
716 mutants by fluorescence polarization (FP). Alanine substitution is performed at K286 in
717 the wild type and mutants (D39A, E263A, N38A, Y58A and N157A) for this assay to
718 prevent substrate digestion during the experiment. (D) NendoU activity profiles for the
719 mutants related to oligomeric assembly.

720

721 **FIG 7 Effects of Mn^{2+} and Mg^{2+} on MERS-Nsp15.** (A) Catalytic rate profile for the
722 effects of Mn^{2+} on the activity of MERS-Nsp15. (B) Nsp15 (K286A)-RNA binding
723 profiles for Nsp15 with increasing Mn^{2+} concentration determined via fluorescence
724 polarization. (C) Catalytic rate profile for the effects of Mg^{2+} on the activity of

725 MERS-Nsp15. (D) Nsp15 (K286A)-RNA binding profiles for Nsp15 with increasing
726 Mg^{2+} concentration determined via fluorescence polarization.

727

728 **FIG 8 Influence of MERS-CoV Nsp8 and the Nsp7/Nsp8 complex on MERS-Nsp15.**

729 (A) Pull-down assays detecting the interaction of the Nsp12/Nsp15, Nsp8/Nsp15 or
730 Nsp8/Nsp15 mutants. (B) MST binding curves for the titration of fluorescently labeled
731 Nsp15 into Nsp8 (green) and Nsp12 (orange). Error bars showing SDs are calculated
732 from triplicate experiments. (C) Determination of the binding affinities of Nsp15 with
733 Nsp7 (black) and the Nsp7/Nsp8 complex (blue) via MST assays. (D) Effects of Nsp8
734 and the Nsp7/Nsp8 complex on the endoribonuclease activity of MERS-Nsp15. (E)
735 Effects of Nsp8 and the Nsp7/Nsp8 complex on the catalytic rate of Nsp15 mutants.

736

737

738

739

740

741

742

743

744

745

746

747

748

749 TABLES

750 Table 1 Data collection and refinement statistics.

Parameters (Data collection statistics)	MERS-Nsp15
Data collection statistics	
Cell parameters	
a (Å)	145.6
b (Å)	145.6
c (Å)	96.7
α, β, γ (°)	90.0, 90.0, 120.0
Space group	<i>H3</i>
Wavelength used (Å)	0.9798
Resolution (Å)	50.0–2.70 (2.75–2.70) ^c
No. of all reflections	222,454 (9,905)
No. of unique reflections	21,016 (1,065)
Completeness (%)	100.0 (100.0)
Average I/σ(I)	10.6 (2.33)
CC _{1/2}	0.952(0.796)
R _{merge} ^a (%)	10.4 (69.9)
Refinement statistics	
No. of reflections used (σ(F) > 0)	19,908
R _{work} ^b (%)	17.5
R _{free} ^b (%)	24.7
r.m.s.d. bond distance (Å)	0.011
r.m.s.d. bond angle (°)	1.453
Average B-value (Å ²)	44.62
No. of protein atoms	5,484
No. of ligand atoms	17
No. of solvent atoms	252
Ramachandran plot	
res. in favored regions (%)	93.66
res. in allowed regions (%)	6.19
res. in outlier regions (%)	0.15

751 ^a $R_{merge} = \frac{\sum_h \sum_l |I_{lh} - I_h|}{\sum_h \sum_l I_h}$ where I_h is the mean of observations I_{lh} of reflection h .752 ^b $R_{work} = \frac{\sum (|F_p(obs) - F_p(calc)|)}{\sum |F_p(obs)|}$. R_{free} is an R factor for a pre-selected subset

753 (5%) of reflections that was excluded in the refinement.

754 ^c Numbers in parentheses are corresponding values for the highest resolution shell.

755

756

757 **Table 2 Catalytic activity and RNA binding properties of wild-type Nsp15 and its**758 **active site mutants.**

MERS-Nsp15	Catalytic rate (nM/s)	Kd value (nM) ^a	Hill coefficient ^b , n
WT	1.25 ± 0.06		
K286A	ND ^c	818.28 ± 50.39	2.24 ± 0.24
H246A	ND	916.47 ± 102.13	2.07 ± 0.53
Y339A	Very low	1029.04 ± 102.73	2.16 ± 0.44
H231A	ND	811.01 ± 51.00	3.11 ± 0.64
S290A	0.83 ± 0.02	1156.49 ± 94.12	2.38 ± 0.37
F285A	1.34 ± 0.06	678.63 ± 36.75	2.72 ± 0.43
F285S	1.63 ± 0.07	616.28 ± 33.09	2.39 ± 0.34
T241A	ND	997.11 ± 121.47	2.30 ± 0.64
T241Q	1.17 ± 0.04	798.96 ± 53.70	2.44 ± 0.47
R341A	ND	1037.28 ± 72.79	2.57 ± 0.44
R341K	0.61 ± 0.06	807.61 ± 51.92	2.65 ± 0.51

759 ^{a,b} All Nsp15 mutants for the FP assays harbored the K286A mutation to avoid the
760 possible digestion of the RNA substrate. The Kd value and Hill coefficient of the
761 wild-type protein were determined and are represented by mutant K286A. The means ±
762 SDs of the Kd and Hill coefficient values shown here were obtained by fitting the data to
763 the Hill equation.

764 ^c Not detected.

765

766

767

768

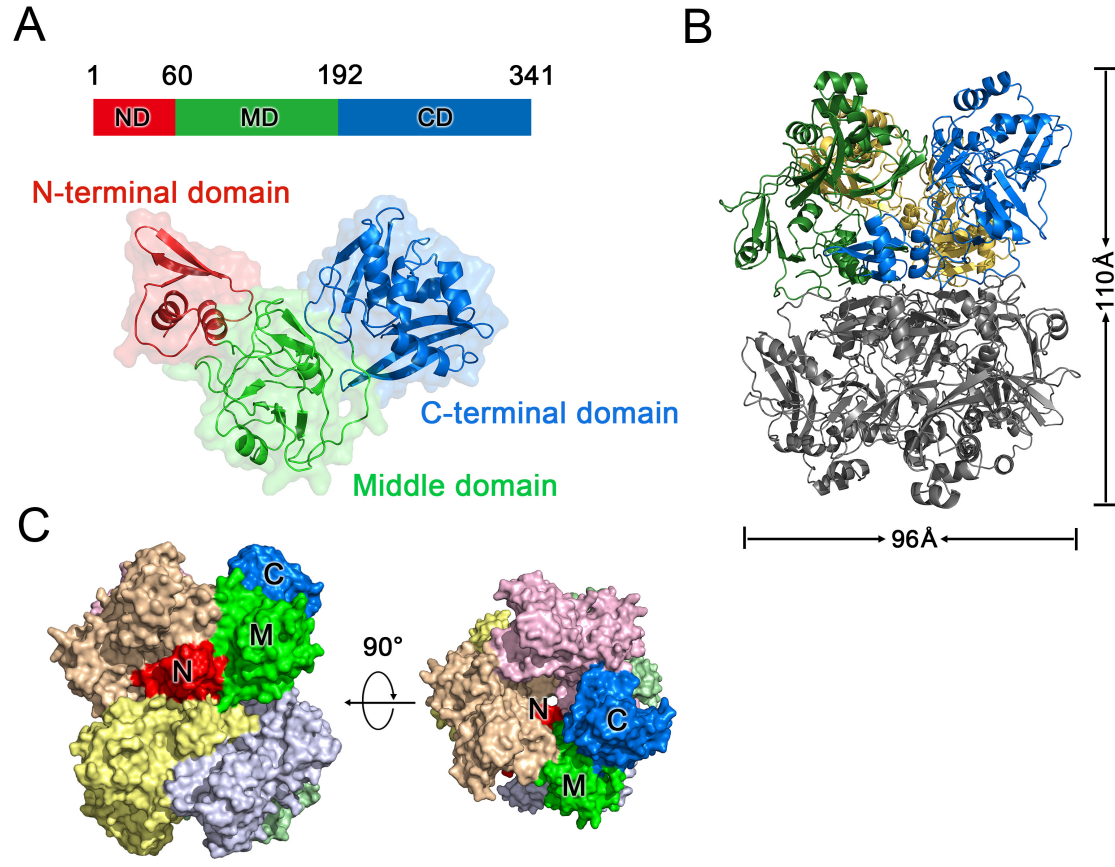
769

770 **Table 3 Catalytic activity and RNA binding properties of wild-type Nsp15 and its**
 771 **subunit interface mutants.**

MERS-Nsp15	Catalytic rate (nM/s)	Kd value (nM) ^a	Hill coefficient ^b , n
WT	1.25 ± 0.06		
K286A	ND ^c	818.28 ± 50.39	2.24 ± 0.24
N38A	0.38 ± 0.04	ND	ND
D39A	1.37 ± 0.04	626.22 ± 24.80	2.15 ± 0.17
N157A	ND	ND	ND
Y58A	0.25 ± 0.03	ND	ND
E263A	0.89 ± 0.06	1013.43 ± 77.38	2.09 ± 0.20

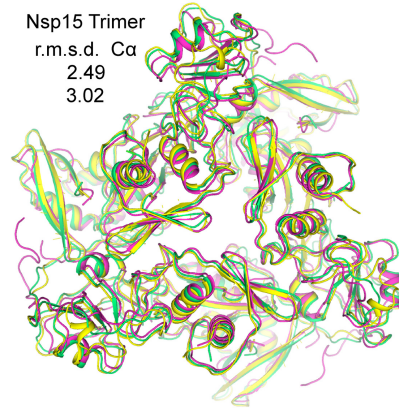
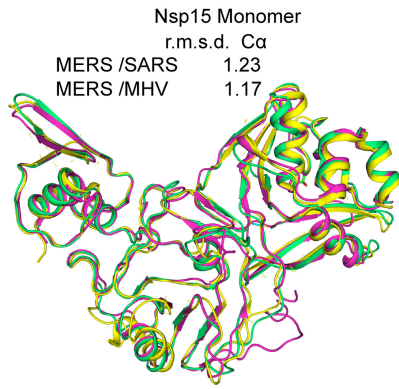
772 ^{a,b} All Nsp15 mutants for the FP assays harbored K286A mutation to avoid digestion of
 773 the RNA substrate. The Kd value and Hill coefficient of the wild-type protein were
 774 measured and are represented by mutant K286A. The means ± SDs of the Kd and Hill
 775 coefficient values shown here were obtained by fitting the data to the Hill equation.

776 ^c Not detected.



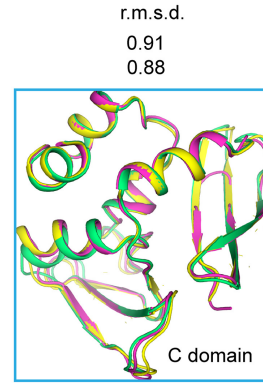
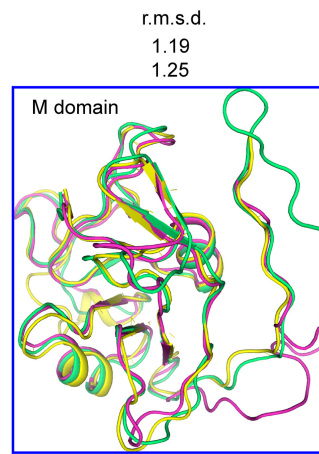
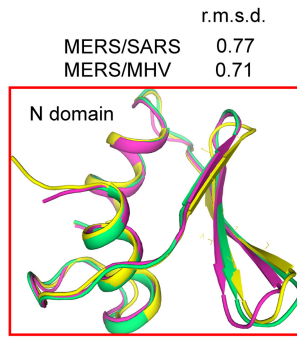
A

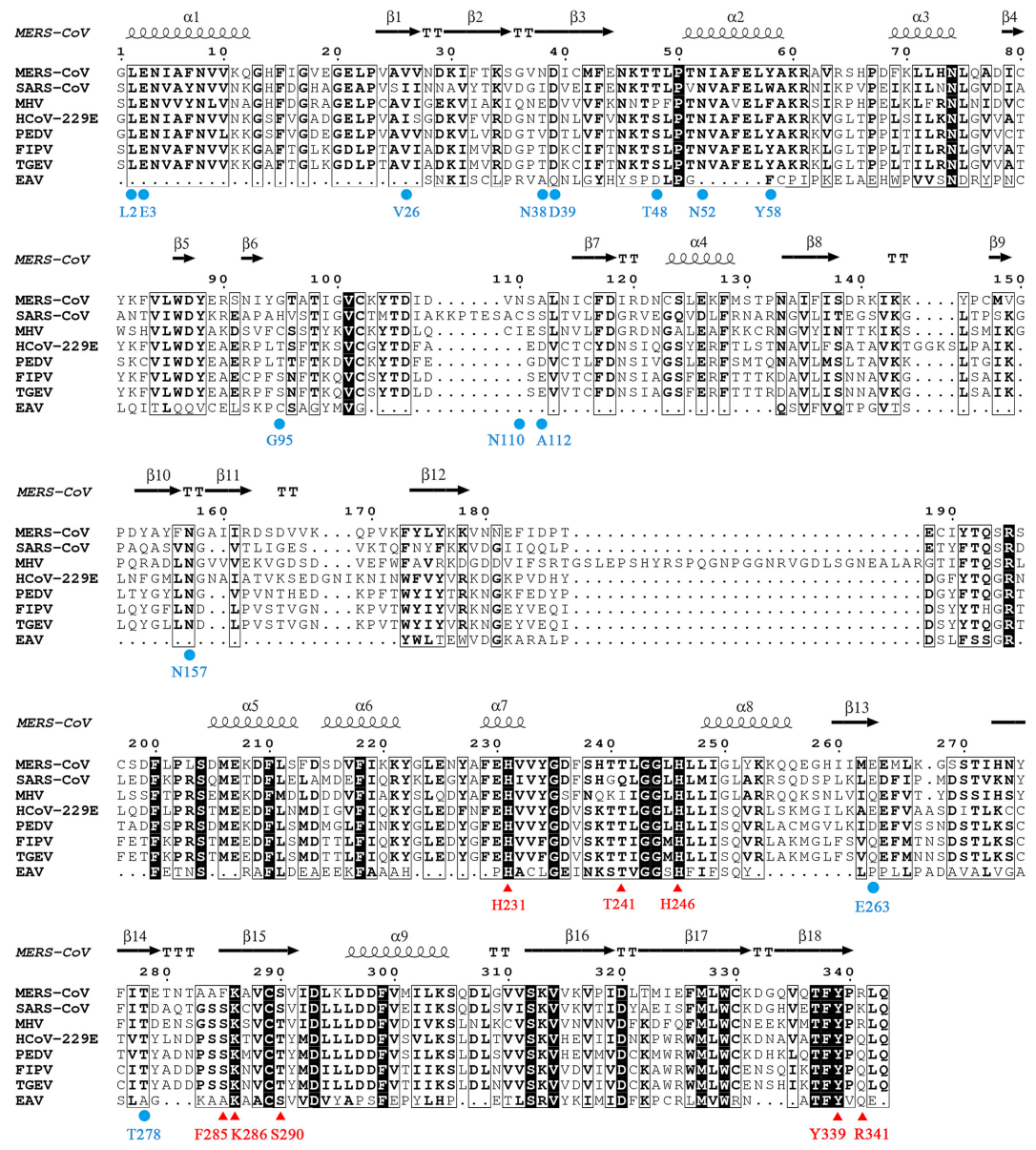
■ MERS-Nsp15
 ■ SARS-Nsp15
 ■ MHV-Nsp15

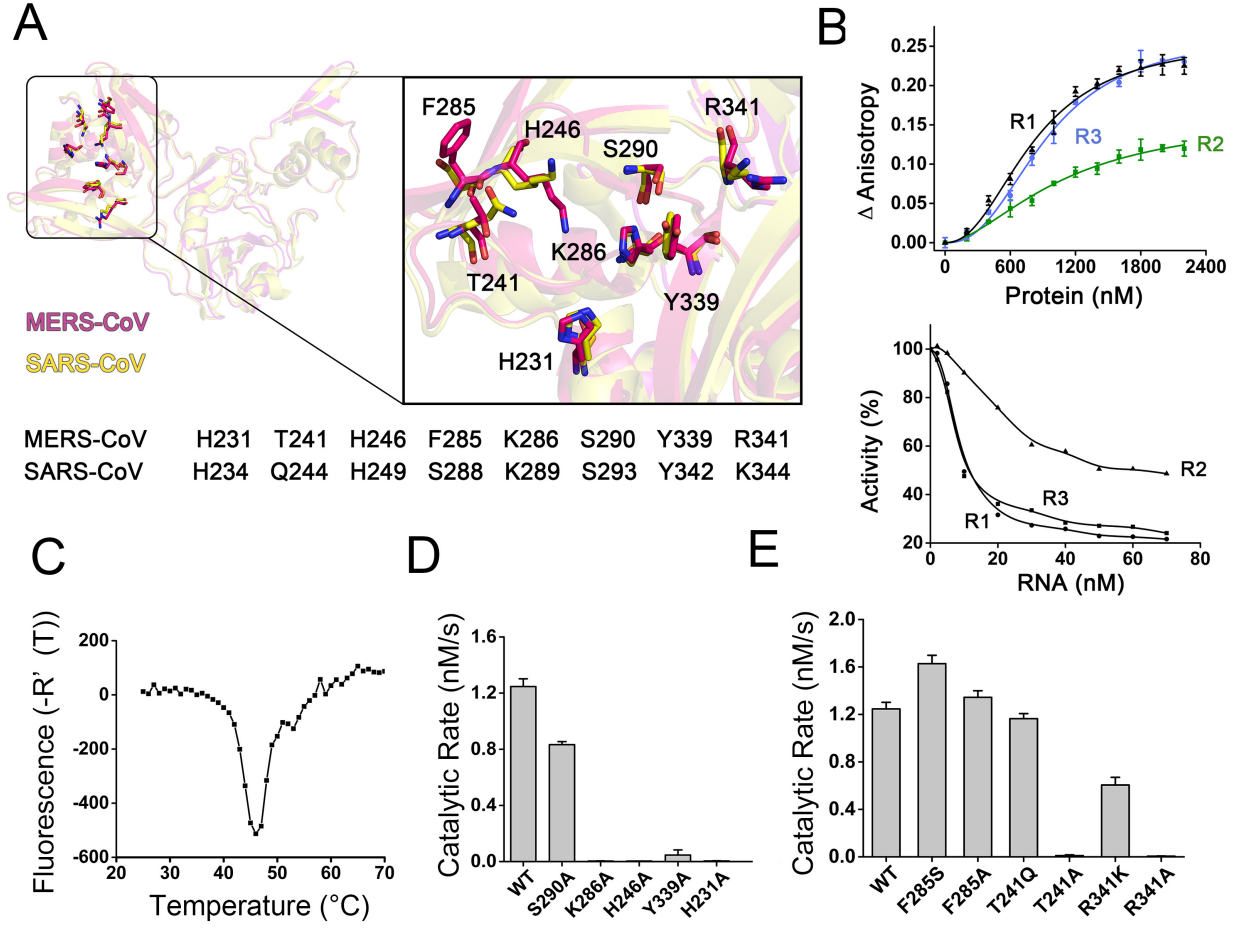


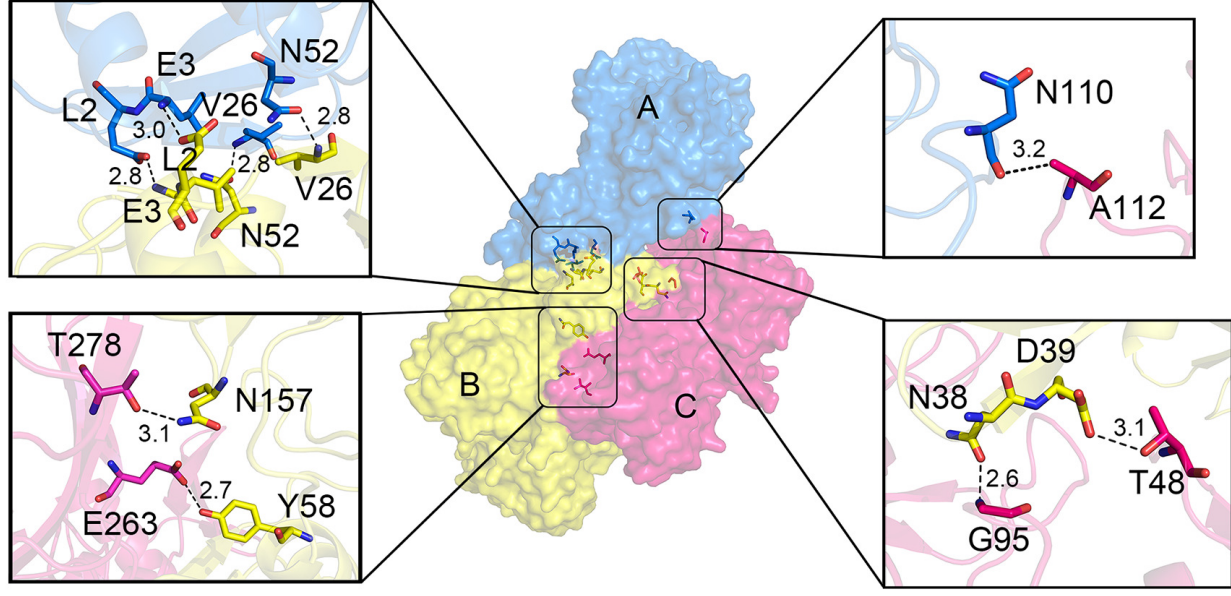
B

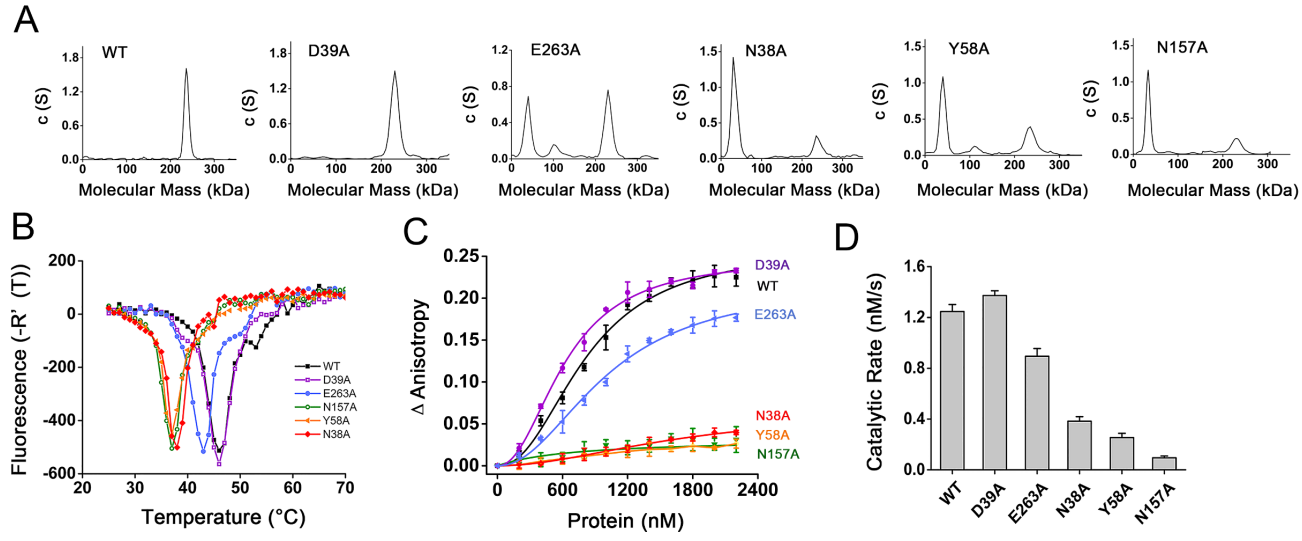
■ MERS-Nsp15
 ■ SARS-Nsp15
 ■ MHV-Nsp15



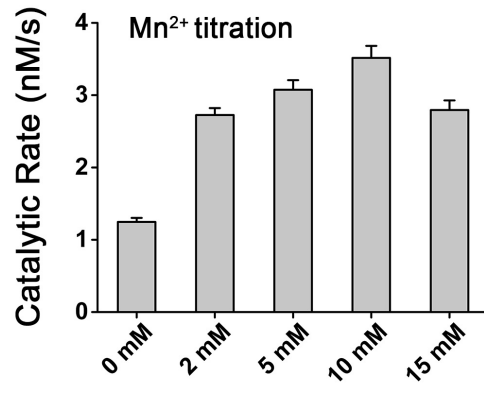




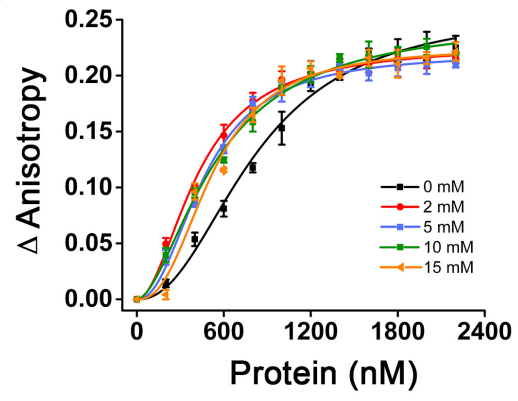




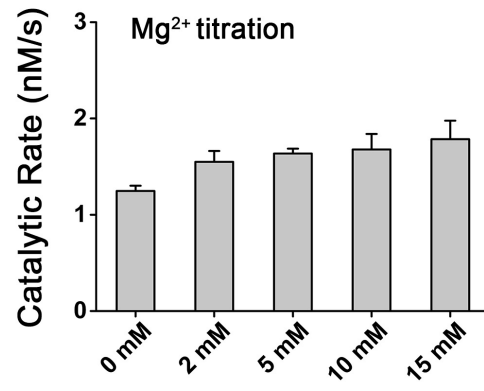
A



B



C



D

